THE JOURNAL OF PHYSICAL CHEMISTRY C
A JOURNAL OF THE AMERICAN CHEMICAL SOCIETY

Open Access
This article is licensed under CC-BY 4.0

pubs.acs.org/JPCC
Article

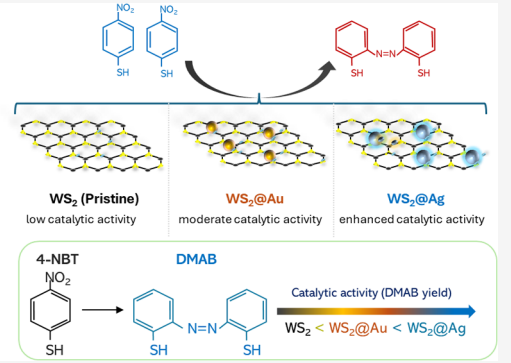
Plasmonic Metal Nanostructures Foster the Catalytic Performance of 2D Dichalcogenide Nanomaterials

Swati J. Patil and Dmitry Kurouski*

Cite This: J. Phys. Chem. C 2026, 130, 15385−15391
Read Online

ACCESS | Metrics & More | Article Recommendations | Supporting Information

ABSTRACT: Transition metal dichalcogenides (TMDs) are novel materials with unique optical, electrical, and chemical properties. These properties are determined by a band gap in the infrared and visible regions of the electromagnetic spectrum. A growing body of evidence indicates that TMDs can perform light-driven catalysis of chemical reactions. Furthermore, the rate and yield of such catalytic reactions can be altered by hybridization of TMDs with metallic nanostructures. However, the underlying mechanisms of such catalysis remain unclear, as does the extent to which the catalytic properties of TMDs can be modified by the metallic nanostructures. In this study, we utilized tip-enhanced Raman spectroscopy (TERS), a novel imaging approach with nanometer spatial resolution, to investigate how hybridization of tungsten disulfide (WS_2) two-dimensional nanostructures with gold (Au) and silver (Ag) nanostructures alters their catalytic properties. Specifically, we measured the yield of *p,p′*-dimercaptoazobisbenzene (DMAB) formed on the surfaces of WS_2, WS_2@Au, and WS_2@Ag decorated with 4-nitrobenzenethiol (4-NBT). Our results show that Ag nanostructures substantially enhanced DMAB-associated Raman response on WS_2, whereas the enhancement observed on WS_2@Au was considerably less pronounced. These results indicate that metallic nanostructures can be used to enhance the catalytic properties of TMDs. Our findings also indicate that the enhancement effect directly depends on the nature of the metal nanostructures hybridized with TMDs.



Metallic nanostructures can interact with light, generating localized surface plasmon resonances (LSPRs), which are coherent oscillations of conduction electrons.[1−4] Upon decay, LSPRs produce both heat and hot carriers, which are highly energetic, short-lived species that can be directly or indirectly injected into molecular orbitals of molecules present on the nanostructure surfaces.[5−8] These charge transfer processes can trigger chemical transformations, a phenomenon known as plasmon-driven chemistry.[9,10] These chemical transformations include, but are not limited to, hydrogen and oxygen splitting, oxidation of 4-aminothiophenol (4-ATP), and conversion of 4-nitrobenzenethiol (4-NBT) to *p,p′*-dimercaptoazobisbenzene (DMAB),[11,12] as well as cleavage of carbon−carbon (C−C),[10] nitrogen−nitrogen (N═N),[13] and gold−sulfur (Au−S) bonds.[14−16]

It has also been shown that the catalytic performance of nanostructures can be enhanced by coupling plasmonic (antenna) metals with catalytic (reactor) metals.[17−21] In such cases, plasmonic metals harvest light to generate hot carriers. These highly energetic species are subsequently transferred to the catalytic nanostructures, which, in turn, facilitate chemical transformations.[16,22] The use of platinum (Pt) or palladium (Pd) as catalytic metals has significantly expanded the spectrum range of chemical reactions performed by such heterostructures.[17−21]

Over the past few years, two-dimensional (2D) transition metal dichalcogenides (TMDs) have attracted the interest of chemists and physicists due to their unique optical, chemical, and electronic properties.[36−38] These properties of TMDs are influenced by thier tunable band gaps in the visible and infrared parts of the electromagnetic spectrum.[12,19] Furthermore, their relatively simplicity of fabrication has made TMDs widely used in optoelectronics,[27,28] optical modulation,[29] photosensing,[30] and semiconductor devices, and sensors.[31−35,20−22] In addition, 2D TMDs exhibit unique catalytic properties. An et al.[23] showed that an MXene-based Au@Ag@Pd/Ti_3C_2 photocatalyst could be used for light-driven hydrogenation of nitroaromatics. Lambin and co-workers found that molybdenum disulfide (MoS_2) flakes could catalyze the photocatalytic reduction of 4-NBT to DMAB,[24] a chemical reaction that had previously been observed only for plasmonic metals.[25] Expanding on these findings, our group showed that the catalytic reactivity of TMDs could be enhanced by

Received: July 16, 2026
Revised: October 7, 2026
Accepted: October 9, 2026
Published: October 22, 2026



ACS Publications
© 2026 The Authors. Published by American Chemical Society

https://doi.org/10.1021/acs.jpcc.6c04761
J. Phys. Chem. C 2026, 130, 15385−15391

Downloaded from pubs.acs.org/jpccck/article-pdf/130/44/15385/6895293/acs.jpcc.6c04761.pdf by TEXAS A&M UNIV COLG STATION user on 09 November 2026

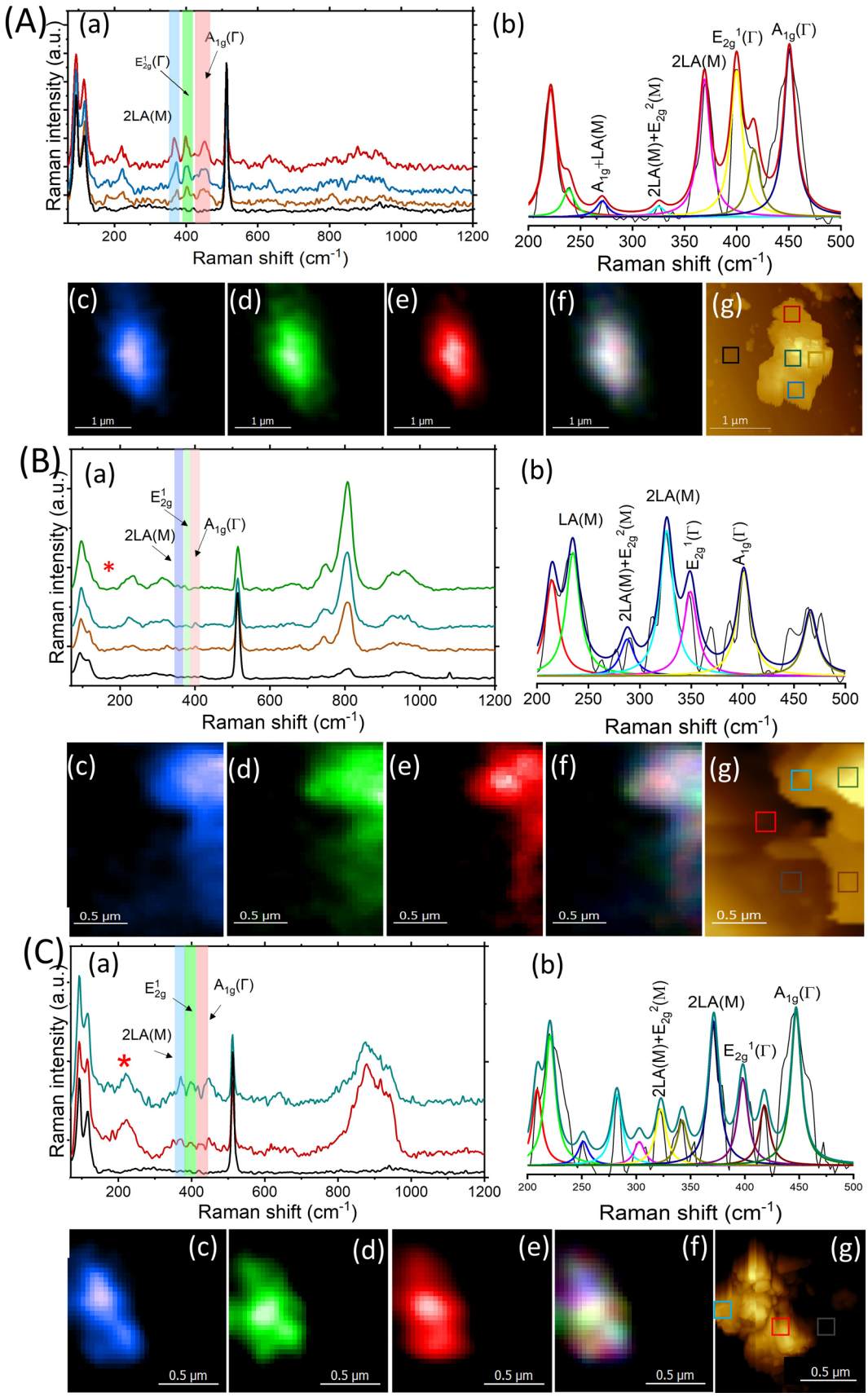


Figure 1. TER spectra (a, b) acquired from WS_2 (A), WS_2@Au (B), and WS_2@Ag (C) TMDs together with corresponding TER maps (c−e) showing the intensities of 2LA (blue), E_{2g} (green), and A_{1g} (red) modes, as well as an overlay map (f) of all three modes. The corersponding AFM image (g) shows the analyzed nanostructure. Scale bars are 1 μm (A) and 0.5 μm (B, C).

https://doi.org/10.1021/acs.jpcc.6c04761
J. Phys. Chem. C 2026, 130, 15385−15391

Downloaded from pubs.acs.org/jpcccck/article-pdf/130/44/15385/6895293/acs.jpcc.6c04761.pdf by TEXAS A&M UNIV COLG STATION user on 09 November 2026

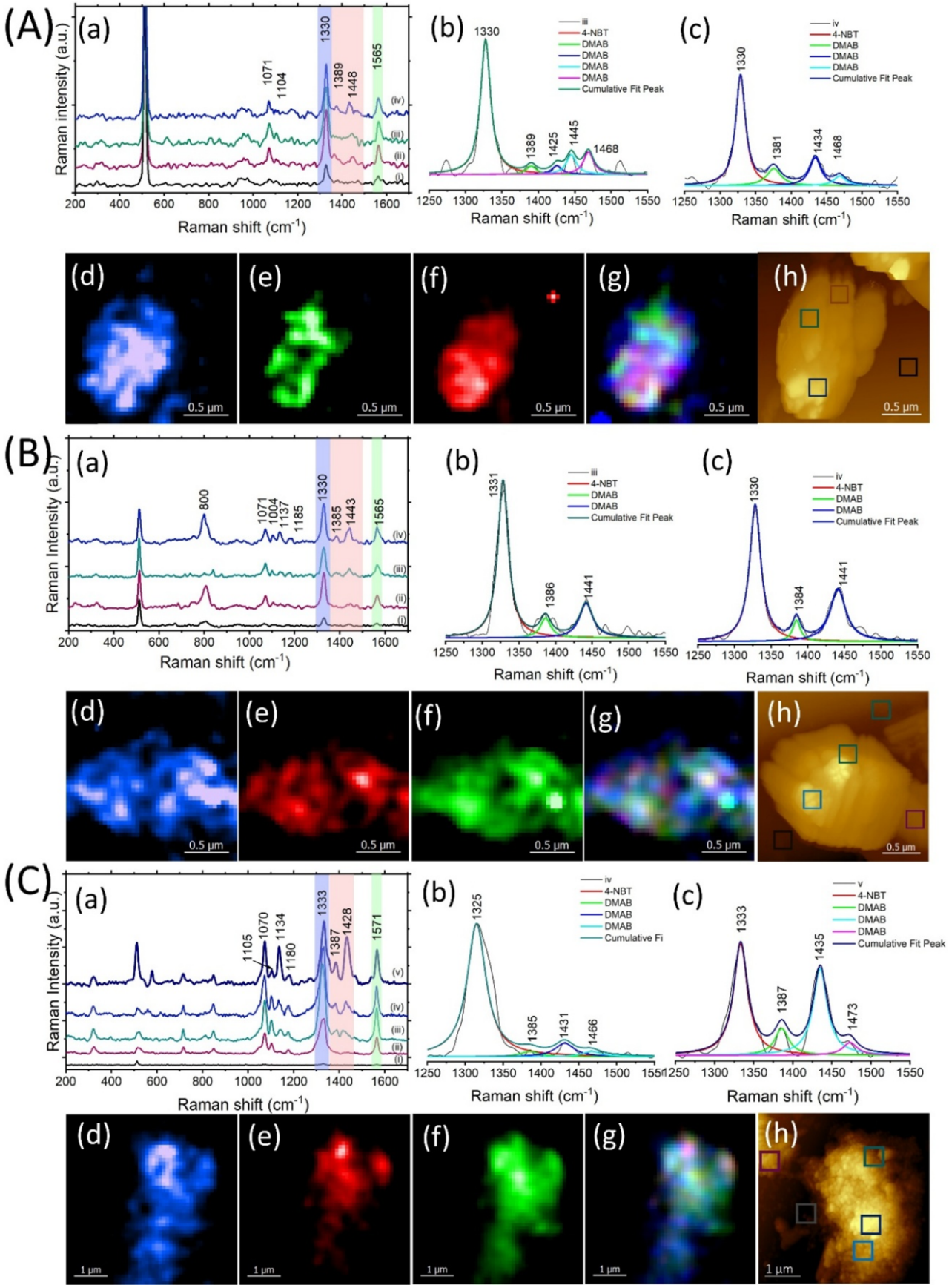


Figure 2. TER spectra (a–c) acquired from WS_2 (A), WS_2@Au (B), and WS_2@Ag (C) along with the corresponding TER maps (d–f) showing the intensities of 4-NBT bands at 1330 cm^{-1} (blue) and 1565 cm^{-1} (green) and DMAB bands at 1385–1443 cm^{-1} (red), as well as an overlay map (g) of all all three signals. The corresponsing AFM image (h) shows the analyzed nanostructure, with squares indicating the locations where spectra

https://doi.org/10.1021/acs.jpcc.6c04761
J. Phys. Chem. C 2026, 130, 15385–15391

Downloaded from pubs.acs.org/jpcccck/article-pdf/130/44/15385/6895293/acs.jpcc.6c04761.pdf by TEXAS A&M UNIV COLG STATION user on 09 November 2026

Figure 2. continued

(a) were acquired. Scale bars are 0.5 μm (A, B) and 1 μm (C). The resolution of each TERS image was 10 nm per pixel, and the spectra acquisition time was 0.5 s per pixel.

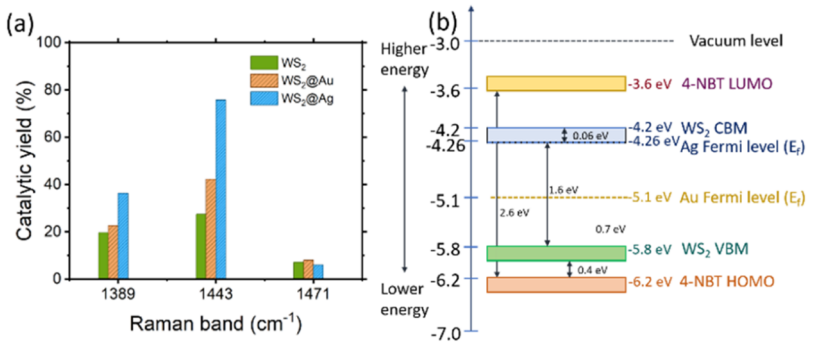


Figure 3. (a) Histograms of relative Raman intensities associated with 4-NBT (1330 cm^{-1}) and DMAB (1389 and 1441 cm^{-1}) obtained from TER spectra of WS_2, WS_2@Au, and WS_2@Ag. (b) Schematic energy-level diagram showing the Fermi levels, WS_2 band edges, and 4-NBT molecular orbitals based on reported literature values.

hybridization with Pd nanoparticles (NPs).[26] Using tip-enhanced Raman spectroscopy (TERS), we also demonstrated that the central regions of tungsten disulfide (WS_2) nanoplates and their Pd hybrids (WS_2@Pd) exhibited greater reactivity than their edges.[26]

In TERS, the scanning probe is brought close to the sample surface and illuminated with light.[27−32] This generates LSPRs at the probe apex surface, which, in turn, amplify Raman scattering from molecules located beneath the probe.[33−38] Enhancement factors of 10^4−10^6 reported to date enables single-molecule sensing.[13,14] It should be noted that the electric field in such a sample-probe junction is confined to a pico-volume cavity, which enables subnanometer spatial resolution upon TERS imaging.[16,39−41] Therefore, TERS can be used to probe chemical reactions, molecular charging, multipolar Raman scattering, and preferred molecular orientations at surfaces.[20,37,42] The strong LSPR and efficient hot-carrier generation observed for silver (Ag) nanoparticles align with foundational studies by Brongersma and co-workers, who reported superior field localization and catalytic efficiency in Ag compared with gold (Au) systems.[8] TERS mapping at the nanoscale, as demonstrated by Zenobi and Van Duyne, further allows us to resolve these differences in catalytic performance. Using TERS, Li and co-workers found that Ag-based systems typically exhibit higher enhancement factors due to stronger plasmonic responses, whereas Au-based systems offer superior chemical stability and reproducibility.[43,44] However, it extent to which hybridization of TMDs with such metals could alter the chemical reactivity of these novel nanomaterials remained unclear. Within this framework, our results provide system-specific confirmation and spatial insights that reinforce and extend established plasmonic mechanisms. In the present study, we used TERS to characterize the chemical structure of synthesized WS_2, WS_2@Au, and WS_2@Ag 2D TMDs. We evaluated DMAB-associated Raman response on these nanomaterials following 4-NBT decoration systematically assessing their TERS performance in Raman signal enhancement and plasmon-driven DMAB formation. By combining spectral analysis with spatial mapping, this study elucidates plasmonic coupling, hotspot distribution, and interfacial interactions that govern nanoscale detection and catalysis, contributing to the advancement of hybrid platforms for high-sensitivity nanoscale spectroscopic applications. TERS analysis of WS_2, WS_2@Au, and WS_2@Ag revealed vibrational bands assigned to A_{1g}-LA(M) at 225−240 cm^{-1}, 2LA-$E_{2g}{}^2$(M) at ∼265 cm^{-1}, 2LA(M) at ∼340 cm^{-1}, $E_{2g}{}^1$ (M) mode at ∼355 cm^{-1}, and A_{1g} (Γ) mode at 417 cm^{-1} (Figure 1). The strong in-plane $E_{2g}{}^1$ mode was associated with in-plane vibrations of S atoms relative to the W atoms. The observed A_{1g} (Γ) mode was assigned to the out-of-plane vibration of S atoms. The vibrational mode at ∼417 cm^{-1} was also attributed to a second-order process that involved the longitudinal acoustic phonons at the M point (LA(M)). The strong intensity of the 2LA(M) vibration in the acquired TER spectra suggested the multilayered nature of the synthesized WS_2, WS_2@Au, and WS_2@Ag nanosheets. We also observed changes in the intensities of the A_{1g}-LA(M), 2LA-$E_{2g}{}^2$, $E_{2g}{}^1$ (M), and A_{1g} (Γ) bands in the spectra acquired from WS_2@Au and WS_2@Ag (Figure 1B,C) compared with those acquired from WS_2 (Figure 1A). These spectroscopic changes suggest coupling between the nanoparticles and 2D TMDs. The observed differences further suggest that this coupling depends on the identity of the metallic nanoparticle.

WS_2 nanosheets selected for analysis had an average thickness of ∼150 nm, with surface roughness ranging from ∼30 to 50 nm, as determined by AFM (Figure S1). Each TERS spectrum was collected with a 0.5 s acquisition time per pixel and a spatial resolution of 10 nm. For each sample type WS_2, WS_2@Au, and WS_2@Ag—a minimum of 10 nanosheets were analyzed, and TERS maps were acquired at 320−350 spatial points per nanosheet.

Next, we utilized TERS to determine the yield of DMAB as well as areas of its formation on the surfaces of WS_2, WS_2@Au, and WS_2@Ag (Figure 2). The Raman spectra highlight the characteristic peaks of 4-NBT (blue and green) and DMAB (red), clearly providing the molecular transformation and catalytic activity across the different WS_2 samples. We observed that pristine WS_2 exhibited very weak photocatalytic activity for the reduction of 4-NBT to DMAB. However, the presence of characteristic DMAB peaks on WS_2 nanosheets confirms plasmon-driven catalytic DMAB formation, with notably stronger DMAB yield at the central regions compared

Downloaded from pubs.acs.org/jpcccck/article-pdf/130/44/15385/6895293/acs.jpcc.6c04761.pdf by TEXAS A&M UNIV COLG STATION user on 09 November 2026

https://doi.org/10.1021/acs.jpcc.6c04761
J. Phys. Chem. C 2026, 130, 15385−15391

with the edges (Figure 2d–f). These results are consistent with the previously reported findings by our group. Spatial TERS mapping shows that multiple vibrational modes are detected in the same localized regions, suggesting spatial corelations between their Raman responses. It should be noted that the Si itself exhibits vibrational signatures of 4-NBT. This is expected because 4-NBT was deposited on WS_2, WS_2@Au, and WS_2@Ag nanostructures previously deposited onto Si substrates.

The results (Figure 2B,C) demonstrate the strong potential of the WS_2@Au and WS_2@Ag TMDs for plasmon-enhanced Raman detection and nanoscale catalytic transformations. The wide-range Raman spectra reveal the coexistence of intrinsic WS_2 vibrational modes and prominent peaks associated with DMAB, suggesting that these semiconductor–metal hybrid structure support catalytic activity. Furthermore, DMAB-associated Raman signals were observed not only in the central regions of the nanostructure, but also across the TMD sheets (1384 and 1441 cm^{-1}). The spectral deconvolution results (Figure 2(b,c)) further support this transformation by resolving the characteristic Raman bands of 4-NBT and DMAB, thereby distinguishing the products from its precursor molecule.

To ensure consistency and enable quantitative comparisons, TERS maps were generated for both 4-NBT and DMAB using the intensities of characteristic fingerprint peaks (1330 cm^{-1} for 4-NBT; 1389 and 1441 cm^{-1} for DMAB) (Figure 3a). The catalytic yield plot presents the DMAB/4-NBT intensity ratio as an indictor of product formation relative to the reactant, enabling a more accurate assessment of catalytic activity for WS_2, WS_2@Au, and WS_2@Ag. For WS_2, low-catlytic DMAB yield confirms that WS_2 alone exhibits limited catalytic activity, which may be associated with its weak plasmonic response and limited ability to generate the localized electromagnetic fields required to drive the 4-NBT to DMAB transformation. We found that Au hybridization resulted in only a slight increase in the DMAB yield, whereas Ag functionalization produced a nearly three-fold enhancement. These results suggest that plasmonic coupling in WS_2@metal systems enhances the observed Raman response associated with DMAB formation, ca with WS_2@Ag showing the strongest sensitivity and catalytic efficiency, while WS_2@Au exhibits a more stable but moderate enhancement.

To rationalize the enhanced catalytic activity response observed for WS_2@Ag compared with WS_2@Au, Figure 3b presents the relative energy level alignment of WS_2, Ag, Au, and 4-NBT based on values reported in previous studies.[20,45,46] The superior performance of WS_2@Ag maybe associated with a combination of plasmonic, electronic, and structural factors. This energy diagram suggests that the Fermi level of Ag and the WS_2 conduction band minimum (CBM) are more closely aligned with the lowest unoccupied molecular orbital (LUMO) of 4-NBT than is the Au Fermi level, potentially facilitating hot electron transfer and promoting DMAB formation.[17−21]

The AFM image (Figure S1) shows that WS_2@Ag exhibits greater surface roughness than WS_2@Au or pristine WS_2, potentially creating additional plasmonic hot spots. These Ag-induced surface features may enhance local electromagnetic fields and promote DMAB formation, consistent with the broader and more intense DMAB signals observed in the WS_2@Ag TERS maps (Figure 2C). These surface features contributes to enhanced plasmonic field localization and provide additional active sites for chemical transformation. In our previous study, finite-difference time-domain (FDTD) calculations were used to understand why Ag NPs exhibited greater photocatalytic reactivity than AuNPs.[44] These simulations showed that Ag NPs generated substantially stronger plasmonic near-fields than AuNPs, a difference arising from the intrinsic dielectric properties of the metals. These results sugges tthat the superior catalytic reactivity of WS_2@Ag hybrids, compared with WS_2@Au, maybe related to the fundamental physical characteristics of Ag, which can supports tronger electromagnetic field enhancement and more efficient plasmon-driven processes.

It should be noted that the Si substrate also exhibited vibrational signatures associated with 4-NBT (Figure 2). This is expected because 4-NBT was deposited on WS_2, WS_2@Au, and WS_2@Ag TMDs that had previously been deposited onto Si substrates. The contribution of the TER probe to the observed DMAB yield on WS_2, WS_2@Au, and WS_2@Ag TMDs cannot be fully eliminated. However, Lambin et al. examined the catalytic reactivity of MoS_2 flakes using confocal Raman spectroscopy, and our group further confirmed these findings using TERS, with both studies reporting low catalytic activity for pristine MoS_2.[24,26] We further demonstrated that functionalization of WS_2 nanoplates with Pd significantly enhanced catalytic reactivity.[26] Comparative TERS imaging of WS_2 and WS_2@Pd showed a marked increase in the DMAB yield for the hybrid, suggesting that the observed differences cannot be attributed solely to the scanning probe. Additionally, our nanoinfrared (nano-IR) spectroscopy experiments, which do not rely on visible light excitation, yielded results consistent with those obtained using TERS, further supporting this interpretation.[26] Based on these results, these observations suggest that although the influence of the TERS probe cannot be entirely excluded, its effect on the measured catalytic reactivity of these nanomaterials is negligible.

In conclusion, our findings suggest that plasmonic nanostructures significantly enhance the catalytic reactivity of TMDs, with the magnitude of enhancement strongly depending on the chemical nature of the hybridized NPs. Specifically, Ag decoration of WS_2 produced a nearly three fold increase in the DMAB yield compared with the pristine material and a substantially greater enhancement than Au decoration, highlighting the key roles of both plasmonic properties and energy-level alignment. These results are consistent with our previous observations for other metal–TMD hybrids and highlight the potential of nanoparticle engineering to modulate the catalytic behavior of two-dimensional materials.[26] A similar trend was observed for 4,4′-BPDT formation on MoS_2 and MoS_2@Au,[47] further suggesting that NP hybridization is a versatile strategy for enhancing the catalytic performance of TMDs.

■ ASSOCIATED CONTENT

Supporting Information

The Supporting Information is available free of charge at https://pubs.acs.org/doi/10.1021/acs.jpcc.6c04761.

Detailed description of experimental procedures, as well as height profiles of the nanostructures (PDF)

■ AUTHOR INFORMATION

Corresponding Author

Dmitry Kurouski − *Department of Biochemistry and Biophysics, Texas A&M University, College Station, Texas 77843, United States; Department of Chemistry, Texas*

https://doi.org/10.1021/acs.jpcc.6c04761
J. Phys. Chem. C 2026, 130, 15385−15391

Downloaded from pubs.acs.org/jpccck/article-pdf/130/44/15385/6895293/acs.jpcc.6c04761.pdf by TEXAS A&M UNIV COLG STATION user on 09 November 2026

A&M University, College Station, Texas 77843, United States; orcid.org/0000-0002-6040-4213; Phone: 979-458-3778; Email: dkurouski@tamu.edu

Author

Swati J. Patil − *Texas A&M High Plain AgriLife Research and Extension Center, Canyon, Texas 79015, United States;* orcid.org/0000-0002-3619-2783

Complete contact information is available at: https://pubs.acs.org/10.1021/acs.jpcc.6c04761

Notes

The authors declare no competing financial interest.

■ ACKNOWLEDGMENTS

We are grateful to AgriLife Research of Texas A&M for the provided financial support. We also acknowledge Governor's University Research Initiative (GURI) grant program of Texas A&M University, GURI Grant Agreement No. 12-2016, M1700437.

■ REFERENCES

(1) Sharma, B.; Frontiera, R. R.; Henry, A. I.; Ringe, E.; Van Duyne, R. P. SERS: Materials, applications, and the future. *Mater. Today* **2012**, *15* (1−2), 16−25.
(2) Xiao, L.; Schultz, Z. D. Spectroscopic Imaging at the Nanoscale: Technologies and Recent Applications. *Anal. Chem.* **2018**, *90* (1), 440−458.
(3) Xie, W.; Schlucker, S. Surface-enhanced Raman spectroscopic detection of molecular chemo- and plasmo-catalysis on noble metal nanoparticles. *Chem. Commun.* **2018**, *54*, 2326−2336.
(4) Patil, S. J.; Lomonosov, V.; Ringe, E.; Kurouski, D. Tip-Enhanced Raman Imaging of Plasmon-Driven Coupling of 4-Nitrobenzenethiol on Au-Decorated Magnesium Nanostructures. *J. Phys. Chem. C* **2023**, *127* (16), 7702−7706.
(5) Moskovits, M. Surface roughness and the enhanced intensity of Raman scattering by molecules adsorbed on metals. *J. Chem. Phys.* **1978**, *69* (9), 4159−4161.
(6) King, F. W.; Van Duyne, R. P.; Schatz, G. C. Theory of Raman scattering by molecules adsorbed on electrode surfaces. *J. Chem. Phys.* **1978**, *69* (10), 4472−4481.
(7) Wustholz, K. L.; Henry, A.-I.; McMahon, J. M.; Freeman, R. G.; Valley, N.; Piotti, M. E.; Natan, M. J.; Schatz, G. C.; Van Duyne, R. P. Structure− activity relationships in gold nanoparticle dimers and trimers for surface-enhanced Raman spectroscopy. *J. Am. Chem. Soc.* **2010**, *132* (31), 10903−10910.
(8) Jeanmaire, D. L.; Van Duyne, R. P. Surface raman spectroelectrochemistry: Part I. Heterocyclic, aromatic, and aliphatic amines adsorbed on the anodized silver electrode. *J. Electroanal. Chem. Interfacial Electrochem.* **1977**, *84* (1), 1−20.
(9) Cortés, E.; Xie, W.; Cambiasso, J.; Jermyn, A. S.; Sundararaman, R.; Narang, P.; Schlücker, S.; Maier, S. A. Plasmonic hot electron transport drives nano-localized chemistry. *Nat. Commun.* **2017**, *8*, No. 14880.
(10) Huh, H.; Trinh, H. D.; Lee, D.; Yoon, S. How Does a Plasmon-Induced Hot Charge Carrier Break a C−C Bond? *ACS Appl. Mater. Interfaces* **2019**, *11* (27), 24715−24724.
(11) Mukherjee, S.; Zhou, L.; Goodman, A. M.; Large, N.; Ayala-Orozco, C.; Zhang, Y.; Nordlander, P.; Halas, N. J. Hot-electron-induced dissociation of H2 on gold nanoparticles supported on SiO2. *J. Am. Chem. Soc.* **2014**, *136* (1), 64−67.
(12) Zhou, L.; Zhang, C.; McClain, M. J.; Manjavacas, A.; Krauter, C. M.; Tian, S.; Berg, F.; Everitt, H. O.; Carter, E. A.; Nordlander, P.; Halas, N. J. Aluminum nanocrystals as a plasmonic photocatalyst for hydrogen dissociation. *Nano Lett.* **2016**, *16* (2), 1478−1484.
(13) Sun, M.; Zhang, Z.; Kim, Z. H.; Zheng, H.; Xu, H. Plasmonic scissors for molecular design. *Chem. - Eur. J.* **2013**, *19* (44), 14958−14962.
(14) Wang, R.; Li, J.; Rigor, J.; Large, N.; El-Khoury, P. Z.; Rogachev, A. Y.; Kurouski, D. Direct Experimental Evidence of Hot-Carrier-Driven Chemical Processes in Tip-Enhanced Raman Spectroscopy (TERS). *J. Phys. Chem. C* **2020**, *124*, 2238−2244.
(15) Wang, F.; Li, C.; Chen, H.; Jiang, R.; Sun, L. D.; Li, Q.; Wang, J.; Yu, J. C.; Yan, C. H. Plasmonic harvesting of light energy for Suzuki coupling reactions. *J. Am. Chem. Soc.* **2013**, *135* (15), 5588−5601.
(16) Zhou, L.; Martirez, J. M. P.; Finzel, J.; Zhang, C.; Swearer, D. F.; Tian, S.; Robatjazi, H.; Lou, M.; Dong, L.; Henderson, L.; et al. Light-driven methane dry reforming with single atomic site antenna-reactor plasmonic photocatalysts. *Nat. Energy* **2020**, *5*, 61−70.
(17) Sytwu, K.; Vadai, M.; Dionne, J. A. Bimetallic nanostructures: combining plasmonic and catalytic metals for photocatalysis. *Adv. Phys.: X* **2019**, *4* (1), 394−418.
(18) Li, Z.; Kurouski, D. Probing the Redox Selectivity on Au@Pd and Au@Pt Bimetallic Nanoplates by Tip-Enhanced Raman Spectroscopy. *Acs Photonics* **2021**, *8* (7), 2112−2119.
(19) Li, Z.; Kurouski, D. Probing the plasmon-driven Suzuki-Miyaura coupling reactions with cargo-TERS towards tailored catalysis. *Nanoscale* **2021**, *13* (27), 11793−11799.
(20) Li, Z.; Kurouski, D. Tip-Enhanced Raman Analysis of Plasmonic and Photocatalytic Properties of Copper Nanomaterials. *J. Phys. Chem. Lett.* **2021**, *12* (34), 8335−8340.
(21) Patil, S. J.; Kurouski, D. Tip-enhanced Raman imaging of plasmon-driven dimerization of 4-bromothiophenol on nickel-decorated gold nanoplate bimetallic nanostructures. *Chem. Commun.* **2023**, *59* (73), 10976−10979.
(22) Brongersma, M. L.; Halas, N. J.; Nordlander, P. Plasmon-induced hot carrier science and technology. *Nat. Nanotechnol.* **2015**, *10* (1), 25−34.
(23) An, H.; Zhang, H.; Zhang, K.; Cheng, R.; Ling, Y.; Zhang, X.; Deng, C.; Xu, Z.; Yin, Z. Construction of a novel hybrid plasmonic metal-2D MXene catalyst for plasmon-driven photoreduction of nitroaromatics. *Applied Surface Science* **2023**, *613*, 156055.
(24) Lambin, C.; Avilés, M. O.; Jelken, J.; Lagugné-Labarthet, F. Molybdenum Disulfide Flakes as Platforms for the Photoconversion of 4-Nitrothiophenol. *J. Phys. Chem. C* **2023**, *127* (50), 24281−24290.
(25) Rizevsky, S.; Kurouski, D. Tip-Enhanced Raman Imaging of Photocatalytic Processes at the Nanoscale. *J. Phys. Chem. C* **2022**, *126* (35), 14781−14790.
(26) Patil, S. J.; Kurouski, D. Nanoscale Imaging of Palladium-Enhanced Photocatalytic Reduction of 4-Nitrothiophenol on Tungsten Disulfide Nanoplates. *Nano Lett.* **2024**, *24* (41), 13004−13009.
(27) Cai, Z. F.; Merino, J. P.; Fang, W.; Kumar, N.; Richardson, J. O.; De Feyter, S.; Zenobi, R. Molecular-Level Insights on Reactive Arrangement in On-Surface Photocatalytic Coupling Reactions Using Tip-Enhanced Raman Spectroscopy. *J. Am. Chem. Soc.* **2022**, *144* (1), 538−546.
(28) Kumar, N.; Stephanidis, B.; Zenobi, R.; Wain, A. J.; Roy, D. Nanoscale Mapping of Catalytic Activity using Tip-Enhanced Raman Spectroscopy with Protected Tips. *Nanoscale* **2015**, *7*, 7133−7137.
(29) Stöckle, R. M.; Suh, Y. D.; Deckert, V.; Zenobi, R. Nanoscale chemical analysis by tip-enhanced Raman spectroscopy. *Chem. Phys. Lett.* **2000**, *318* (1−3), 131−136.
(30) Chen, C.; Hayazawa, N.; Kawata, S. A. 1.7 nm resolution chemical analysis of carbon nanotubes by tip-enhanced Raman imaging in the ambient. *Nat. Commun.* **2014**, *5*, No. 3312.
(31) Hayazawa, N.; Inouye, Y.; Sekkat, Z.; Kawata, S. Metallized tip amplification of near-field Raman scattering. *Opt. Commun.* **2000**, *183* (1−4), 333−336.
(32) Verma, P. Tip-Enhanced Raman Spectroscopy: Technique and Recent Advances. *Chem. Rev.* **2017**, *117* (9), 6447−6466.
(33) Kurouski, D.; Dazzi, A.; Zenobi, R.; Centrone, A. Infrared and Raman chemical imaging and spectroscopy at the nanoscale. *Chem. Soc. Rev.* **2020**, *49* (11), 3315−3347.

Downloaded from pubs.acs.org/jpcock/article-pdf/130/44/15385/6895293/acs.jpcc.6c04761.pdf by TEXAS A&M UNIV COLG STATION user on 09 November 2026

(34) Kurouski, D.; Mattei, M.; Van Duyne, R. P. Probing Redox Reactions at the Nanoscale with Electrochemical Tip-Enhanced Raman Spectroscopy. *Nano Lett.* **2015**, *15* (12), 7956−7962.
(35) Bhattarai, A.; Crampton, K. T.; Joly, A. G.; Kovarik, L.; Hess, W. P.; El-Khoury, P. Z. Imaging the Optical Fields of Functionalized Silver Nanowires through Molecular TERS. *J. Phys. Chem. Lett.* **2018**, *9* (24), 7105−7109.
(36) Bhattarai, A.; O'Callahan, B. T.; Wang, C. F.; Wang, S.; El-Khoury, P. Z. Spatio-Spectral Characterization of Multipolar Plasmonic Modes of Au Nanorods via Tip-Enhanced Raman Scattering. *J. Phys. Chem. Lett.* **2020**, *11* (8), 2870−2874.
(37) O'Callahan, B. T.; El-Khoury, P. Z. A Closer Look at Tip-Enhanced Raman Chemical Reaction Nanoimages. *J. Phys. Chem. Lett.* **2022**, *13* (17), 3886−3889.
(38) Wang, C. F.; O'Callahan, B. T.; Kurouski, D.; Krayev, A.; Schultz, Z. D.; El-Khoury, P. Z. Suppressing Molecular Charging, Nanochemistry, and Optical Rectification in the Tip-Enhanced Raman Geometry. *J. Phys. Chem. Lett.* **2020**, *11*, 5890−5895.
(39) Zhang, R.; Zhang, Y.; Dong, Z. C.; Jiang, S.; Zhang, C.; Chen, L. G.; Zhang, L.; Liao, Y.; Aizpurua, J.; Luo, Y.; et al. Chemical mapping of a single molecule by plasmon-enhanced Raman scattering. *Nature* **2013**, *498* (7452), 82−86.
(40) Lee, J.; Crampton, K. T.; Tallarida, N.; Apkarian, V. A. Visualizing vibrational normal modes of a single molecule with atomically confined light. *Nature* **2019**, *568* (7750), 78−82.
(41) Tallarida, N.; Lee, J.; Apkarian, V. A. Tip-Enhanced Raman Spectromicroscopy on the Angstrom Scale: Bare and CO-Terminated Ag Tips. *ACS Nano* **2017**, *11* (11), 11393−11401.
(42) Li, Z.; Rigor, J.; Large, N.; El-Khoury, P.; Kurouski, D. Underlying Mechanisms of Hot Carrier-Driven Reactivity on Bimetallic Nanostructures. *J. Phys. Chem. C* **2021**, *125*, 2492−2501.
(43) Li, Z.; Ehtesabi, S.; Gojare, S.; Richter, M.; Kupfer, S.; Grafe, S.; Kurouski, D. Plasmon-Determined Selectivity in Photocatalytic Transformations on Gold and Gold-Palladium Nanostructures. *ACS Photonics* **2023**, *10* (9), 3390−3400.
(44) Li, Z.; Rigor, J.; Ehtesabi, S.; Gojare, S.; Kupfer, S.; Grafe, S.; Large, N.; Kurouski, D. Role of Plasmonic Antenna in Hot Carrier-Driven Reactions on Bimetallic Nanostructures. *J. Phys. Chem. C* **2023**, *127* (46), 22635−22645.
(45) Li, Z.; El-Khoury, P.; Kurouski, D. Tip-Enhanced Raman Imaging of Photocatalytic Reactions on Thermally-Reshaped Gold and Gold-Palladium Microplates. *Chem. Commun.* **2021**, *57* (7), 891−894, DOI: 10.1039/D0CC07060B.
(46) Li, Z.; Kurouski, D. Plasmon-Driven Chemistry on Mono- and Bimetallic Nanostructures. *Acc. Chem. Res.* **2021**, *54* (10), 2477−2487.
(47) Patil, S. J.; Kurouski, D. Nano-RamanandNano-InfraredImagingofDimerizationof 4-Bromothiophenolon2DMolybdenumDisulfideandMolybdenum Disulfide@GoldHybrids. *J. Phys. Chem. C* **2024**, *128*, 16514−16521.

Downloaded from pubs.acs.org/jpccck/article-pdf/130/44/15385/6895293/acs.jpcc.6c04761.pdf by TEXAS A&M UNIV COLG STATION user on 09 November 2026